Prepared for submission to JHEP

$\tau^- \to (3\pi)^- \nu_\tau$ decays with dispersive constraints

Alexander Friedland,[a] **Sergi Gonzàlez-Solís,**[b,c] **Emilie Passemar**[b,c,d]

[a] *SLAC National Accelerator Laboratory, 2575 Sand Hill Road, Menlo Park, CA 94025, USA.*
[b] *Department of Physics, Indiana University, Bloomington, IN 47405, USA.*
[c] *Center for Exploration of Energy and Matter, Indiana University, Bloomington, IN 47408, USA.*
[d] *Theory Center, Thomas Jefferson National Accelerator Facility, Newport News, VA 23606, USA*

E-mail: alexfr@slac.stanford.edu, sgonzal@iu.edu, epassema@indiana.edu

Abstract: The $\tau^- \to (3\pi)^- \nu_\tau$ decays offer a good environment to study the three-pion dynamics. From the point of view of strong interactions, the 3π system in the final state is isolated thus providing a clean laboratory for studying the properties of the produced axial $a_1(1260)$-meson. In this work, we provide a description of the contributing axial-vector form factor that is based on constraints posed by analyticity and unitarity, and by chiral symmetry to a lesser extent, and we probe its application against the measurement of the axial-vector spectral function reported by the ALEPH collaboration in 2014. A satisfactory description of experimental data is achieved working with a twice-subtracted dispersion relation without the need to include other intermediate states than the contributions of the $\rho(770), a_1(1260)$ and $a_1(1640)$ resonances. As a side result, the axial form factor parametrization as extracted from this theoretically clean data will be used as input to describe the axial-vector form factor of the nucleon [1].

Keywords: Hadronic tau decays, Chiral Lagrangians, Dispersion relations.

Contents

1 Introduction

Tau lepton decays provide an advantageous laboratory to test the Standard Model under rather clean conditions. Its exclusive semileptonic decays into a neutrino and hadrons in particular, offer interesting possibilities to investigate the non-perturbative regime of QCD since half of the process is purely electroweak and can be computed straightforwardly. These transitions probe the vector and axial-vector parts of the weak hadronic current between the QCD vacuum and the hadronic final state. Such privileged framework is used to improve our understanding of the hadronization of QCD currents, to study form factors and to extract the physical parameters, mass and width, of the intermediate resonances produced in the decay.

In the understanding of the strong hadron dynamics at low-and-intermediate energies, the spectral functions play a capital role. The n-pion decay modes are the cleanest hadronic channels to test the vector (if n is even) and the axial-vector (if n is odd) spectral functions. The two-pion decay almost saturates the vector spectral function below ~ 1 GeV^2 which, in turn, it is dominated by the visible peak corresponding to the formation of the $\rho(770)$-resonance. The vector spectral function can be related with the pion vector form factor, an object of high physical interest, since it enters the description of many physical process, and that it has been measured in $e^+e^- \to \pi^+\pi^-$ [2–8] and in $\tau \to \pi^-\pi^0\nu_\tau$ [9, 10] and widely studied in the literature (see e.g. Ref. [11] and references therein). On the contrary, the three-pion channel dominates the axial-vector spectral function up to ~ 2 GeV^2 and offers a good environment to study the 3π system under rather clean conditions. This is expected to be in a $J^{PC} = 1^{++}$ state produced predominantly through the $a_1(1260)$ axial vector meson thus offering a laboratory to study its properties more advantageous than the diffractive reaction $\pi p \to \pi\pi\pi p$ [12] where the 3π in the final state shows a more complex dynamical structure[1].

In the past, ARGUS [14], ALEPH [15] and DELPHI [16] have measured the $\tau^- \to (3\pi)^-\nu_\tau$ branching ratio and spectra, while OPAL [17] and CLEO [18, 19] measured the corresponding structure functions. On the theory side, Breit-Wigner models for the participant axial-vector form factor [20–23], with the effects of the $a_1(1260)$ encoded into, have been typically used to describe data until the authors of Refs. [24, 25] abandoned any modelization and provided an Effective Theory based description incorporating the relevant features of QCD in the resonance region. The most recent measurement of the axial-vector spectral function corresponds to the results released by the ALEPH Collaboration in 2005 [26], and the corresponding data have been analyzed by several groups following different approaches [27–29]. In 2014, however, ALEPH made an update [30] of their 2005 data after improving the method to unfold the measured mass spectra from detector effects and correcting previous problems in the correlations between the unfolded mass bins; the statistical bin-to-bin correlations introduced by the unfolding method in the 2005 analysis were not included. As a result, the new data were binned into wider and asymmetric bins with respect to the old one[2] and dropped the number of data points by a factor of ~ 2.

Our aim is to provide an elaborated analysis of this data following a dispersive approach similar to the ones employed for the $\pi\pi$ [11, 31, 32] and $K\pi$ [33] vector form factors, respectively. In our case, the $a_1(1260)$-meson is expected to dominate the 3π axial-vector form factor and elastic unitarity is expected to hold in a good approximation. Our procedure is organized according to the fulfillment of unitarity and analyticity constraints. We start with a representation of the axial form factor corresponding to a Breit-Wigner with only the $a_1(1260)$-width resummed into the resonance propagator, and follow with a dispersive Breit-Wigner expression that includes the real part of the unitary corrections, that is, the off-shell propagation of 3π intermediate states. The effects of the first radial excitation i.e. the $a_1(1640)$-meson, will be also taken into account and discussed accordingly. The dispersive Breit-Wigner parametrization allows us to get a model for the phase that we use as input for the two-times subtracted dispersion relation that completes our representation of the form factor. As we will see, our parametrization provides a good phenomenological result when confronted to the experimental ALEPH data [30].

As a benefit of our study, we are in a position to use our parametrization, extracted from this theoretically clean $\tau^- \to (3\pi)^-\nu_\tau$ data, as input to describe the axial-vector form factor of the nucleon [1].

This paper is organized as follows. The hadronic matrix element and the participating form factor are defined in section 2, where the differential decay distribution and axial spectral function in terms of the latter are also given. In section 3, we discuss different parametrizations of the axial-vector form factor organized according to their increasing fulfillment of unitarity and analyticity constraints. In sections 4 and 5, we probe our

[1] The interested reader is referred to Ref. [13] for a discussion on the discrepancy in the extraction of the $a_1(1260)$ resonance parameters from tau decays and from pion diffraction.

[2] See Fig. 3 of Ref. [30] for a graphical comparison between the new-and-old unfolded spectral functions.

parametrizations against the ALEPH 2014 spectral function data. Finally, in section 6 we present our conclusions.

2 Matrix elements and decay width

The generic amplitude for a three meson decay of the τ is given by

$$\mathcal{M}(\tau^- \to (PPP)^- \nu_\tau) = \frac{G_F}{\sqrt{2}} |V_{ij}| \bar{u}_{\nu_\tau} \gamma_\mu (1-\gamma_5) u_\tau \langle (PPP)^- | (V-A)^\mu | 0 \rangle \,, \tag{2.1}$$

where G_F is the Fermi constant and $|V_{ij}|$ is the corresponding element of the CKM matrix for the transition. The last term in Eq. (2.1) is the hadronic matrix element that can be written in terms of four form factors, $F^A_{1,2,3}$ and F^V_4, as [34]

$$\begin{aligned}\langle (P(p_1)P(p_2)P(p_3))^- | (V-A)^\mu | 0 \rangle &= V_1^\mu F_1^A(Q^2, s_1, s_2) + V_2^\mu F_2^A(Q^2, s_1, s_2) \,, \\ &+ Q^\mu F_3^A(Q^2, s_1, s_2) + i V_4^\mu F_4^V(Q^2, s_1, s_2) \,, \end{aligned} \tag{2.2}$$

where

$$V_1^\mu = \left(g^{\mu\nu} - \frac{Q^\mu Q^\nu}{Q^2} \right) (p_1 - p_3)_\nu \,, \quad V_2^\mu = \left(g^{\mu\nu} - \frac{Q^\mu Q^\nu}{Q^2} \right) (p_2 - p_3)_\nu \,, \tag{2.3}$$

$$V_4^\mu = \varepsilon^{\mu\alpha\beta\gamma} p_{1\alpha} p_{2\beta} p_{3\gamma} \,, \quad Q^\mu = (p_1 + p_2 + p_3)^\mu \,, \quad s_i = (Q - p_i)^2 \,, \tag{2.4}$$

and where the upper indices on the form factors stand for the participating current i.e. axial-vector (A) and vector (V). In the decomposition given in Eq. (2.2), $F_1^A(Q^2, s_1, s_2)$ and $F_2^A(Q^2, s_1, s_2)$ are the axial-vector form factors that drive a $J^P = 1^+$ transition, while $F_3^A(Q^2, s_1, s_2)$ is the pseudoscalar form factor that carries $J^P = 0^-$ degrees of freedom. Finally, $F_4^V(Q^2, s_1, s_2)$ is the vector form factor that has $J^P = 1^-$.

In terms of these form factors, the Q^2 differential decay rate distribution can be written as (in the vanishing neutrino mass limit)

$$\begin{aligned}\frac{d\Gamma(\tau^- \to (PPP)^- \nu_\tau)}{dQ^2} &= \frac{G_F^2 |V_{ij}|^2}{128 (2\pi)^5 M_\tau} \left(\frac{M_\tau^2}{Q^2} - 1 \right)^2 \int_{s_{1,\min}}^{s_1^{\max}} ds_1 \int_{s_{2,\min}}^{s_2^{\max}} ds_2 \\ &\times \left[W_{SA} + \frac{1}{3} \left(1 + 2 \frac{Q^2}{M_\tau^2} \right) (W_A + W_B) \right] \,, \end{aligned} \tag{2.5}$$

where $s_1 = (p_2 + p_3)^2$, $s_2 = (p_1 + p_3)^2$ and $s_3 = (p_1 + p_2)^2 \equiv Q^2 - s_1 - s_2 + m_1^2 + m_2 + m_3^2$, and with the hadronic structure functions, W_{SA} and $W_{A,B}$, given by

$$W_{SA} = \left[Q^\mu F_3^A(Q^2, s_1, s_2) \right] \left[Q_\mu F_3^A(Q^2, s_1, s_2) \right]^* = Q^2 |F_3^A(Q^2, s_1, s_2)|^2 \,, \tag{2.6}$$

$$\begin{aligned} W_A = &- \left[V_1^\mu F_1^A(Q^2, s_1, s_2) + V_2^\mu F_2^A(Q^2, s_1, s_2) \right] \times \\ &\left[V_{1\mu} F_1^A(Q^2, s_1, s_2) + V_{2\mu} F_2^A(Q^2, s_1, s_2) \right] \,, \end{aligned} \tag{2.7}$$

$$W_B = \left[V_{4\mu} F_4^V(Q^2, s_1, s_2) \right] \left[V_4^\mu F_4^V(Q^2, s_1, s_2) \right]^* \,. \tag{2.8}$$

The limits of integration in Eq. (2.5) are given by

$$s_{2,\min}^{\max}(Q^2, s_1) = \frac{1}{4s}\Big\{ \left(Q^2 + m_1^2 - m_2^2 - m_3^2\right)^2 - \Big[\lambda^{1/2}(Q^2, s_1, m_3^2) \mp \lambda^{1/2}(m_1^2, m_2^2, s_1)\Big]^2 \Big\}, \tag{2.9}$$

$$s_{1,\min} = (m_1 + m_2)^2 , \quad s_1^{\max} = \left(\sqrt{Q^2} - m_3\right)^2 , \tag{2.10}$$

$$Q^2_{\min} = (m_1 + m_2 + m_3)^2 , \quad Q^2_{\max} = (M_\tau - m_\nu)^2 , \tag{2.11}$$

where $\lambda(a, b, c) = (a + b - c)^2 - 4ab$.

For $\tau^- \to (3\pi)^-\nu_\tau$, only the axial-vector current is allowed due to G-parity conservation and thus we have no vector contribution i.e. $F_4^V(Q^2, s_1, s_3) = 0$. Bose symmetry under the interchange of the two identical pions of the final state implies $F_1^A(Q^2, s_1, s_2) = F_2^A(Q^2, s_2, s_1) \equiv F^A(Q^2, s_1, s_2)$. Meanwhile, conservation of axial-vector current in the chiral limit imposes that $F_3^A(Q^2, s_1, s_2)$ must vanish with the square of the pion mass and therefore its contribution will be very much suppressed and can be safely neglected. Therefore, the 3π state is assumed to be dominated by a state of angular momentum one.

For definiteness, we describe the remaining axial vector form factor for the channel $\tau^- \to \pi^-\pi^+\pi^-\nu_\tau$, and use the isospin symmetry relation [35, 36]

$$\begin{aligned} F^A(Q^2, s_1, s_2) &\equiv F^A_{\pi^-\pi^+\pi^-}(Q^2, s_1, s_2) \\ &= F^A_{\pi^0\pi^0\pi^-}(Q^2, s_1, s_3) - F^A_{\pi^0\pi^0\pi^-}(Q^2, s_2, s_3) - F^A_{\pi^0\pi^0\pi^-}(Q^2, s_1, s_2) , \end{aligned} \tag{2.12}$$

to describe the mode $\tau^- \to \pi^0\pi^0\pi^-\nu_\tau$.

Finally, the axial-vector hadronic current takes the form

$$J_A^\mu = F^A(Q^2, s_1, s_2)V_1^\mu + F^A(Q^2, s_2, s_1)V_2^\mu , \tag{2.13}$$

while the calculation of the decay rate Eq. (2.5) is reduced to the computation of the axial-vector spectral function, $a_1(Q^2)$, and it can be written as

$$\frac{d\Gamma(\tau^- \to \pi^-\pi^-\pi^+\nu_\tau)}{dQ^2} = \frac{G_F^2|V_{ud}|^2}{32\pi^2 M_\tau}\left(M_\tau^2 - Q^2\right)^2 \left(1 + \frac{2Q^2}{M_\tau^2}\right) a_1(Q^2) , \tag{2.14}$$

where

$$a_1(Q^2) = \frac{1}{768\pi^3}\frac{1}{Q^4}\int_{s_{1,\min}}^{s_1^{\max}} ds_1 \int_{s_{2,\min}}^{s_2^{\max}} ds_2\, W_A . \tag{2.15}$$

For comparison of theory and experiment, it is useful to define the ratio of the partial decay width of $\tau^- \to (3\pi)^-\nu_\tau$ over the $\tau^- \to e^-\bar{\nu}_e\nu_\tau$ partial width

$$\frac{\Gamma(\tau^- \to (3\pi)^-\nu_\tau)}{\Gamma(\tau^- \to e^-\bar{\nu}_e\nu_\tau)}\frac{1}{N_{\text{events}}}\frac{dN_{\text{events}}}{dQ^2} = \frac{6\pi|V_{ub}|^2 S_{EW}}{M_\tau^2}\left(1 - \frac{Q^2}{M_\tau^2}\right)^2 \left(1 + 2\frac{Q^2}{M_\tau^2}\right) a_1(Q^2) , \tag{2.16}$$

where $(1/N_{\text{events}})(dN_{\text{events}}/dQ^2)$ is the normalized invariant mass-squared distribution, S_{EW} accounts for short-distance electroweak radiative corrections, and the CKM matrix element $|V_{ub}| = 0.97418 \pm 0.00019$ [37].

For the evaluation of the axial-vector form factor, $F^A(Q^2, s_1, s_2)$, we follow Ref. [22] as an initial approach and assume that this current is dominated by the a_1 and its subsequent decay to $\rho\pi$ through the decay chain $\tau \to \nu_\tau a_1 \to \nu_\tau \rho\pi \to 3\pi$. Under this ansatz, the form factor can be written as

$$F^A(Q^2, s_1, s_2) = F_{a_1}(Q^2) F_\rho(s_2) \,, \tag{2.17}$$

where $F_{a_1}(Q^2)$ accounts for the resonant structure of the produced $a_1(1260)$-meson while $F_\rho(s_i)$ stands for the subchannel $\rho \to \pi\pi$ decay with the requirement $F_\rho(s_i) \to 1$ as $s_i \to 0$. To describe the contribution of the ρ-meson resonance shape, we use [32, 38]

$$F_\rho(s) = \frac{m_\rho^2}{m_\rho^2 - s + \kappa_\rho(s)\mathrm{Re}\left(A_\pi(s,\mu) + \frac{1}{2}A_K(s,\mu)\right) - i m_\rho \Gamma_\rho(s)} \,, \tag{2.18}$$

where $A_P(s,\mu)$ are the chiral loop functions given by (we take $\mu = m_\rho$)

$$A_P(s,\mu^2) = \log\frac{m_P^2}{\mu^2} + \frac{8m_P^2}{s} - \frac{5}{3} + \sigma_P^3(s)\log\left(\frac{\sigma_P(s)+1}{\sigma_P(s)-1}\right) \,, \tag{2.19}$$

with

$$\sigma_P(s) = \sqrt{1 - \frac{4m_P^2}{s}} \,. \tag{2.20}$$

In Eq. (2.18), $\kappa_\rho(s)$ and the energy-dependent width $\Gamma_\rho(s)$ are given by [38]

$$\kappa_\rho(s) = \frac{\gamma_\rho}{m_\rho}\frac{s}{\pi\left(\sigma_\pi^3(m_\rho^2) + 1/2\sigma_K^3(m_\rho^2)\right)} \,, \tag{2.21}$$

$$\Gamma_\rho(s) = \gamma_\rho \frac{s}{m_\rho^2}\frac{\sigma_\pi^3(s) + 1/2\sigma_K^3(s)}{\sigma_\pi^3(m_\rho^2) + 1/2\sigma_K^3(m_\rho^2)} \,. \tag{2.22}$$

The quantities m_ρ and γ_ρ are model parameters and do not correspond to the physical $\rho(770)$ mass and width. For our study, we use the parameters m_ρ and γ_ρ tuned such that the $\rho(770)$-pole mass and width, $M_\rho^{\text{pole}} = 762.0(3)$ MeV and $\Gamma_\rho^{\text{pole}} = 143.0(2)$ MeV [11], are reproduced[3]. These are found to be $m_\rho = 797.5$ MeV and $\gamma_\rho = 196.0$ MeV. We would like to point out here that the form presented in Eq. (2.18) fulfills analyticity since both the real and imaginary part of loop integral function are resummed in the propagator of the ρ-meson resonance. This represents and improved treatment of the ρ-meson line shape with respect to the works of Refs. [18, 24, 25, 29], where the real part of the unitary corrections was not taken into account.

The form factor in Eq. (2.17) is equivalent to write the current in Eq. (2.13) in the form

$$J_A^\mu = F_{a_1}(Q^2)\left[F_\rho(s_2)V_{1\mu} + F_\rho(s_1)V_{2\mu}\right] \,, \tag{2.23}$$

[3]We consider the pole mass and width as the relevant resonance properties since one expects the pole parameters to be essentially model independent.

and the isospin relation Eq. (2.12) between the modes $\pi^-\pi^+\pi^-$ and $\pi^0\pi^0\pi^-$ reduces to

$$F^A(Q^2, s_1, s_2) = -F^A_{\pi^0\pi^0\pi^-}(Q^2, s_1, s_2)\,, \tag{2.24}$$

thus giving the same predictions for both decay channels (in the isospin limit). In [22], the normalization of $F_{a_1}(Q^2)$ was chosen such that for $Q^2 \to 0$ one recovers the ChPT prediction at $\mathcal{O}(p^2)$ [39]

$$J^\mu_A|^{\mathcal{O}(p^2)}_{\mathrm{ChPT}} = -\frac{2\sqrt{2}}{3F_\pi}\left(V_{1\mu} + V_{2\mu}\right)\,. \tag{2.25}$$

To fulfill Eq. (2.25), the form factor $F_{a_1}(Q^2)$ in Eq. (2.23) can be written as:

$$F_{a_1}(Q^2) = -\frac{2\sqrt{2}}{3F_\pi} f_{a_1}(Q^2)\,, \tag{2.26}$$

where $f_{a_1}(Q^2)$ parametrizes the Q^2 behavior of the a_1 resonance with the property $f_{a_1}(Q^2) \to 1$ as $Q^2 \to 0$.

In this framework, the axial spectral function Eq. (2.15) reads:

$$a_1(Q^2) = \frac{1}{768\pi^3}\left(-\frac{2\sqrt{2}}{3F_\pi}\right)^2 |f_{a_1}(Q^2)|^2 \frac{g(Q^2)}{Q^2}\,, \tag{2.27}$$

where

$$\begin{aligned} g(Q^2) = \frac{1}{Q^2}\int_{s_{1,\mathrm{min}}}^{s_1^{\mathrm{max}}} ds_1 \int_{s_{2,\mathrm{min}}}^{s_2^{\mathrm{max}}} ds_2 \Big\{ & - V_1^2|F_\rho(s_2)|^2 - V_2^2|F_\rho(s_1)|^2 \\ & - 2V_1V_2 \mathrm{Re}\left[F_\rho(s_1)(F_\rho(s_2))^*\right]\Big\}\,, \end{aligned} \tag{2.28}$$

with

$$-V_1^2 = (s_2 - 4m_\pi^2) + (s_3 - s_1)^2/(Q^2)\,, \tag{2.29}$$

$$-V_2^2 = (s_2 - 4m_\pi^2) + (s_3 - s_2)^2/(Q^2)\,, \tag{2.30}$$

$$-V_1V_2 = (Q^2/2 - s_3 - m_\pi^2/2) + (s_3 - s_1)(s_3 - s_2)/(4Q^2)\,. \tag{2.31}$$

However, as pointed out in Ref. [24], the current in Eq. (2.23) has a drawback, while it was constructed to fulfill the lowest order behaviour of ChPT (cf. Eq. (2.25)) it does not reproduces the tree-level next-to-leading order result [40]

$$\begin{aligned} F^A(Q^2, s_1, s_2)|^{\mathcal{O}(p^4)_{\mathrm{tree}}}_{\mathrm{ChPT}} = -\frac{2\sqrt{2}}{3F_\pi}\Bigg(& 1 + \frac{4(2L_1 + L_3)}{F_\pi^2}(s_3 - 2m_\pi^2) + \frac{4L_2}{F_\pi^2}(s_2 - 2s_1 + 2m_\pi^2) \\ & + \frac{4(2L_4 + L_5)m_\pi^2}{F_\pi^2} + \frac{2L_9 Q^2}{F_\pi^2}\Bigg)\,, \end{aligned} \tag{2.32}$$

and thus it is not consistent with the chiral symmetry of QCD. To further illustrate this fact, let us take the (vector) resonance saturation of the $\mathcal{O}(p^4)$ couplings[4] [41]

$$2L_1 = L_2 = \frac{1}{4}L_9 = \frac{F_\pi^2}{8M_V^2}\,, \tag{2.33}$$

that yields a form factor of the form:

$$F^A(Q^2, s_1, s_2)|^{\mathcal{O}(p^4)_{\rm tree}}_{\rm ChPT} = -\frac{2\sqrt{2}}{3F_\pi}\left(1 + \frac{3s_2}{2M_V^2}\right)\,, \tag{2.34}$$

or, what is equivalent, an axial-vector current of the form:

$$J_A^\mu|^{\mathcal{O}(p^4)_{\rm tree}}_{\rm ChPT} = -\frac{2\sqrt{2}}{3F_\pi}\left[\left(1 + \frac{3s_2}{2M_V^2}\right)V_{1\mu} + \left(1 + \frac{3s_1}{2M_V^2}\right)V_{2\mu}\right]\,. \tag{2.35}$$

This low-energy behaviour is not reproduced by the model of Eq. (2.23), where the hadronic current in the limit $s_{1,2} \ll M_V^2$ behaves as

$$J_A^\mu|_{s_{1,2}\ll M_V^2} = -\frac{2\sqrt{2}}{3F_\pi}\left[\left(1 + \frac{s_2}{M_V^2}\right)V_{1\mu} + \left(1 + \frac{s_1}{M_V^2}\right)V_{2\mu}\right]\,. \tag{2.36}$$

An advisable solution to this drawback may come from using dispersion relations with subtractions. In the vicinity of the origin $Q^2 = 0$, the form factor can be represented by its Taylor expansion

$$F_{a_1}(Q^2) = -\frac{2\sqrt{2}}{3F_\pi}\left(1 + \lambda_1 Q^2 + \cdots\right)\,, \tag{2.37}$$

where λ_1 can be related into a determination of the low-energy constants of ChPT thus fulfilling the chiral expansion of the axial-vector form factor.

For our study, we will explore different parametrizations for $f_{a_1}(Q^2)$ organized according to the fulfillment of analyticity and unitarity arguments, and the chiral symmetry of QCD to some extent. These are presented in the following section.

3 Representations of the axial-vector form factor

3.1 Non-dispersive Breit-Wigner models

As initial setup approach, we represent the form factor by means of a one single resonance Breit-Wigner

$$f_{\rm BW}^{1\,\rm res}(Q^2) = \frac{m_{a_1}^2}{m_{a_1}^2 - Q^2 - i m_{a_1}\Gamma_{a_1}(Q^2)}\,, \tag{3.1}$$

where, since the participating $a_1(1260)$ resonance is not narrow, we have considered its energy dependent width through

$$\Gamma_{a_1}(Q^2) = \gamma_{a_1}\frac{g(Q^2)}{g(m_{a_1}^2)}\theta(Q^2 - 9m_\pi^2)\,. \tag{3.2}$$

[4]The low-energy constants L_4 and L_5 are saturated by scalar contributions that are neglected in our work and we therefore set them to zero.

The parameters m_{a_1} and γ_{a_1} are the non-physical "mass" and "width" to be determined from fits to the data. We would like to note that these parameters can acquire values different from the physical pole mass and width of the resonance, $M_{a_1}^{\rm pole}$ and $\Gamma_{a_1}^{\rm pole}$, which are determined from the pole positions in the complex plane.

Despite Eq. (3.1) might provide a successful description of data, contributions from the first radial excitation i.e. the $a_1' \equiv a_1(1640)$-meson, might appear on the upper part of the spectrum. To consider these potential effects, we propose to proceed by

$$f_{\rm BW}^{2\,\rm res}(Q^2) = \frac{1}{1+|\kappa|e^{i\phi}}\left[\frac{m_{a_1}^2}{m_{a_1}^2 - Q^2 - im_{a_1}\Gamma_{a_1}(Q^2)} + |\kappa|e^{i\phi}\frac{m_{a_1'}^2}{m_{a_1'}^2 - Q^2 - im_{a_1'}\Gamma_{a_1'}(Q^2)}\right], \tag{3.3}$$

where κ is a parameter that accounts for the mixing between resonances, and it is in general complex thus carrying a phase that we denote by ϕ. However, for our study we will assume κ to be real both for lack of precise experimental data near the tau mass, where the effects of the a_1' can show up, and to avoid introducing a small spurious imaginary part below the $9m_\pi^2$ threshold. We shall return to this point in section 4.

In Eq. (3.3), we assume that the energy dependent width of the a_1' exhibits the same energy behavior than that of the a_1

$$\Gamma_{a_1'}(Q^2) = \gamma_{a_1'}\frac{g(Q^2)}{g(m_{a_1'}^2)}\theta(Q^2 - 9m_\pi^2)\,. \tag{3.4}$$

As the 3π decay offers a limited phase space to extract the mass and width of the a_1' with accurate precision, for our analysis we fix them to their PDG values, $m_{a_1'} = 1647$ MeV and $\gamma_{a_1'} = 254$ MeV [37], while we let $|\kappa|$ as a free parameter to fit.

There are some drawbacks associated with the Breit-Wigner form factor described above. Most importantly, the constraints imposed by analyticity and unitarity are not fully respected. In order to fulfill analyticity, the real part of the unitarity corrections, that accounts for the off-shell propagation of the 3π intermediate states, should be taken into account in the resonance propagator. Moreover, this description might generates artificial poles, and does not incorporates the low-energy constraints from chiral symmetry. Therefore, the extrapolation of this form factor to low-energies should be taken with caution. These limitations explains the need to build more sophisticated descriptions. The use of dispersive parametrizations of the form factor cure most of the aforementioned pathologies, if not all.

3.2 Dispersive Breit-Wigner models

In order to fully fulfill analyticity, we resumme the real part of the loop integrals, that account for the off-shell propagation of 3π intermediate states, in the propagator of the a_1-meson resonance through

$$f_{\rm BW}^{1\,\rm res}(Q^2)|_{\rm disp} = \frac{m_{a_1}^2}{m_{a_1}^2 - Q^2 + \Pi(Q^2)} = \frac{m_{a_1}^2}{m_{a_1}^2 - Q^2 + {\rm Re}\Pi(Q^2) + i{\rm Im}\Pi(Q^2)}, \tag{3.5}$$

where m_{a_1} is the bare or tree level mass of the resonance and $\Pi(Q^2) = \sum_i \Pi_i(Q^2)$ is the (one-particle-irreducible) renormalization term that accounts for the unitary loop corrections.

The sum runs over the loops emerging from the coupling of the resonance to various decay channels. Unitarity relates the imaginary part of $\Pi(Q^2)$ with the partial decay width of the a_1 resonance into mesons in mode i through

$$\mathrm{Im}\Pi(Q^2) = -m_{a_1}\Gamma_{a_1}^{\mathrm{total}}(Q^2) = -m_{a_1}\sum_i \Gamma_{a_1}^i(Q^2)\,. \tag{3.6}$$

The incorporation of the real part $\mathrm{Re}\Pi(Q^2)$ in the denominator of Eq. (3.5) constitutes and improved version of the Breit-Wigner Eq. (3.1) that incorporates unitarity and analyticity constraints. As a result, one can define the running mass of the resonance as

$$m_{a_1}(Q^2) \equiv m_{a_1}^2 + \mathrm{Re}\Pi(Q^2)\,. \tag{3.7}$$

Analyticity relates the imaginary and real parts of $\Pi(q^2)$ through a dispersion relation

$$\mathrm{Re}\Pi(Q^2) = \frac{1}{\pi}\int_{9m_\pi^2}^{\infty} ds'\,\frac{-\mathrm{Im}\Pi(s')}{Q^2-s'}\,. \tag{3.8}$$

From the above equation we see that if $\mathrm{Im}\Pi(Q^2)$ is know up to infinity, we can obtain $\mathrm{Re}\Pi(Q^2)$ and thus fully determine $f_{\mathrm{BW}}^{1\,\mathrm{res}}(Q^2)|_{\mathrm{disp}}$. However, in real physical situations the full width $\Gamma_{a_1}^{\mathrm{total}}(Q^2)$ is usually not know up to arbitrarily large energies as demanded by the dispersive integral of Eq. (3.8). This lack of knowledge can be compensated by introducing subtractions

$$\mathrm{Re}\Pi(Q^2) = \sum_{k=0}^{n-1}\frac{(Q^2-s_0)^k}{k!}\frac{d^k(\mathrm{Re}\Pi(Q^2))}{d(Q^2)^k}\bigg|_{Q^2=s_0} + \frac{(Q^2-s_0)^n}{\pi}\int_{9m_\pi^2}^{\infty} ds'\,\frac{-\mathrm{Im}\Pi(s')}{(s'-s_0)^n(Q^2-s')}\,. \tag{3.9}$$

This has the virtue that increases the powers of Q^2 in the denominator of the integrand thus reducing the importance of the contributions from the high energy region in the integral where $\Gamma_{a_1}^{\mathrm{total}}(Q^2)$ is less well-know. For our study, we perform one subtraction and write

$$f_{\mathrm{BW}}^{1\,\mathrm{res}}(Q^2)|_{\mathrm{disp}} = \frac{m_{a_1}^2 + \mathrm{Re}\Pi_{a_1}(0)}{m_{a_1}^2 - Q^2 + \mathrm{Re}\Pi_{a_1}(Q^2) - i m_{a_1}\Gamma_{a_1}(Q^2)}\,, \tag{3.10}$$

where

$$\mathrm{Re}\Pi_{a_1}(Q^2) = \mathcal{H}_{a_1}(Q^2) - \mathcal{H}_{a_1}(m_{a_1}^2)\,, \tag{3.11}$$

and with

$$\mathcal{H}_{a_1}(Q^2) = -\frac{Q^2}{\pi}\int_{9m_\pi^2}^{s_{\mathrm{cut}}} ds'\,\frac{m_{a_1}\Gamma_{a_1}(s')}{(s')(s'-Q^2)}\,. \tag{3.12}$$

The subtraction in Eq. (3.11) corresponds to the term $\mathcal{H}(m_{a_1}^2)$ and has been chosen such that the running mass and width, Eqs. (3.7) and (3.2), equal the (renormalized) bare mass and nominal width[5]

$$m_{a_1}(Q^2)|_{Q^2=m_{a_1}^2} = m_{a_1}^2\,, \quad \Gamma_{a_1}(Q^2)|_{Q^2=m_{a_1}^2} = \gamma_{a_1}\,. \tag{3.13}$$

[5]Without loss of generality, the running mass can be defined to vanish at some other arbitrary values.

Another important aspect of Eq.(3.12) is the introduction of the integral cutoff $s_{\rm cut}$. By introducing subtractions we increases the power of Q^2 in the denominator of the integrand. However, the high energy part of the integral, where our models cannot be trusted nor measurable since include intermediate states that open above the τ mass, still contributes. This contribution remains as a source of theoretical uncertainty in our results. In order to quantify it, we vary $s_{\rm cut}$ and the corresponding results will be discussed and used as a source of systematic uncertainties. This constitutes an alternative approach different to the ones employed in Refs. [18, 27, 29], where the integral was performed until infinity and a correction form factor introduced *ad hoc* to force a damping of the amplitudes and make the integral converge.

The term $\mathrm{Re}\Pi_{a_1}(0)$ in the numerator of Eq. (3.10) ensures that $f_{\rm BW}^{1\,\rm res}(Q^2)|_{\rm disp} \to 1$ for $Q^2 \to 0$.

Similar to Eq. (3.3), the role of the a_1' is included through

$$f_{\rm BW}^{2\,\rm res}(Q^2)|_{\rm disp} = \frac{1}{1+|\kappa|e^{i\phi}}\left[\frac{m_{a_1}^2+\mathrm{Re}\Pi_{a_1}(0)}{m_{a_1}^2-Q^2+\mathrm{Re}\Pi_{a_1}(Q^2)-im_{a_1}\Gamma_{a_1}(Q^2)}\right.$$
$$\left. + |\kappa|e^{i\phi}\frac{m_{a_1'}^2+\mathrm{Re}\Pi_{a_1'}(0)}{m_{a_1'}^2-Q^2+\mathrm{Re}\Pi_{a_1'}(Q^2)-im_{a_1'}\Gamma_{a_1'}(Q^2)}\right]. \tag{3.14}$$

3.3 Dispersive representation

An important feature the form factor given by Eq. (3.5) possess is that in the elastic approximation i.e. $\mathrm{Im}\Pi(Q^2) \equiv \mathrm{Im}\Pi_{a_1\to 3\pi}(Q^2)$, it is equivalent to the once subtracted Omnès representation [42]

$$f(Q^2) = \exp\left[\frac{Q^2}{\pi}\int_{9m_\pi^2}^{\infty} ds' \frac{\delta(s')}{s'(s'-Q^2-i0)}\right], \tag{3.15}$$

where the phase $\delta(Q^2)$ entering the dispersive integral encodes the physics of the participating resonances. In order to get a model for the phase, we adopt the form factor representation given in Eq. (3.5) and extract the phase from the relation

$$\tan\delta(Q^2) = \frac{\mathrm{Im} f_{\rm BW}^{1\,\rm res}(Q^2)|_{\rm disp}}{\mathrm{Re} f_{\rm BW}^{1\,\rm res}(Q^2)|_{\rm disp}}, \tag{3.16}$$

that it is only valid in the τ decay region ($Q^2 < m_\tau^2$) since the model parameters i.e. m_{a_1} and γ_{a_1}, will be fitted to τ data and therefore one cannot obtain reliable information beyond m_τ^2. Strictly speaking, however, one should integrate the dispersive integral up to infinity. For that, the phase has to be known for all values of $Q^2 > 9m_\pi^2$. This is certainly not our case, since we are using a modelization for the phase $\delta(Q^2)$ given by Eq. (3.16) as input. For the high-energy region, we thus take a conservative interval between 0 and 2π and guide smoothly the phase to π at $Q^2 = m_\tau^2$ through [11]

$$\delta_\infty(Q^2) \equiv \lim_{s\to\infty}\delta(Q^2) = \pi - \frac{a}{b+(Q^2/m_\tau^2)^{3/2}}, \tag{3.17}$$

where a and b are parameters taken such the phase $\psi(s)$ and its first derivative $\psi'(s)$ are continuous at $Q^2 = m_\tau^2$

$$a = \frac{3\left(\pi - \delta(m_\tau^2)\right)^2}{2m_\tau^2\delta'(m_\tau^2)}\,, \quad b = -1 + \frac{3\left(\pi - \delta(m_\tau^2)\right)}{2m_\tau^2\delta'(m_\tau^2)}\,. \tag{3.18}$$

This ensures the correct asymptotic $1/Q^2$ fall-off of the form factor.

In order to diminish the importance of the contributions coming from the high-energy part of the integral where the phase is less well known, one can introduce subtractions. The general solution for n subtractions can be written as

$$f(Q^2) = \mathcal{P}_n(Q^2)\exp\left[\frac{(Q^2-s_0)^n}{\pi}\int_{9m_\pi^2}^{\infty} ds'\frac{\delta(s')}{(s'-s_0)^n(s'-Q^2-i0)}\right]\,, \tag{3.19}$$

with

$$\mathcal{P}(Q^2) = \exp\left[\sum_{k=0}^{n-1}\lambda_k(Q^2-s_0)^k\right]\,, \tag{3.20}$$

and where

$$\lambda_k = \frac{1}{k!}\frac{d^k}{d(Q^2)^k}\log f(Q^2)\bigg|_{Q^2=s_0}\,. \tag{3.21}$$

4 Breit-Wigner fits to the ALEPH spectral function data

The χ^2 function minimized in our fits is defined as

$$\chi^2 = \sum_{i,j=1}^{all}\Delta_i^{\mathrm{ALEPH}}(\mathrm{Cov}_{ij}^{\mathrm{ALEPH}})^{-1}\Delta_j^{\mathrm{ALEPH}}\,, \tag{4.1}$$

with

$$\Delta_k^{\mathrm{ALEPH}} = a_1^{\mathrm{ALEPH}}(Q^2)_k - a_1^{\mathrm{th}}(Q^2)_k\,, \tag{4.2}$$

where $a_1^{\mathrm{ALEPH}}(Q^2)_k$ and Cov_{ij} are, respectively, the ALEPH experimental measurement of the spectral function and the corresponding covariance matrix in the k-th bin, while $a_1^{\mathrm{th}}(Q^2)_k$ is our theoretical description. The number of fitted data points is 74 and 73 for the $\pi^0\pi^0\pi^-$[6] and $\pi^-\pi^+\pi^-$ decay channels, respectively.

We start by fitting Eq. (2.15) to the axial spectral function measured by ALEPH [30] with the non-dispersive Breit-Wigner form factor given in Eq. (3.1). In order to optimize our fits to the data, we did not fix the normalization but rather introduced a scale factor, denoted by $\mathcal{N}$ hereafter, that we have allowed to float in order to reproduce better the branching ratio quoted by ALEPH. The parameters resulting from our first fit take the values

$$m_{a_1} = 1271(4)\,\mathrm{MeV}\,, \quad \gamma_{a_1} = 523(8)\,\mathrm{MeV}\,, \quad \mathcal{N} = 1.59(4)\,, \tag{4.3}$$

[6] The first two points of the $\pi^0\pi^0\pi^-$ mode have been excluded from the minimization since the central values are found to be negative.

with a $\chi^2/\mathrm{dof} = 1.16$ for the $\tau^- \to \pi^0\pi^0\pi^-\nu_\tau$ decay channel, and

$$m_{a_1} = 1243(3)\,\mathrm{MeV}\,, \quad \gamma_{a_1} = 480(7)\,\mathrm{MeV}\,, \quad \mathcal{N} = 1.43(3)\,, \tag{4.4}$$

with a $\chi^2/\mathrm{dof} = 3.11$ for the $\tau^- \to \pi^-\pi^+\pi^-\nu_\tau$ mode.

For our second fit, we include the $a_1(1640)$-meson and use Eq. (3.3). We obtain

$$m_{a_1} = 1236(7)\,\mathrm{MeV}\,, \quad \gamma_{a_1} = 506(10)\,\mathrm{MeV}\,, \quad |\kappa| = 0.16(2)\,, \quad \mathcal{N} = 1.21(6)\,, \tag{4.5}$$

with a $\chi^2/\mathrm{dof} = 0.99$ for $\tau^- \to \pi^0\pi^0\pi^-\nu_\tau$, and

$$m_{a_1} = 1212(4)\,\mathrm{MeV}\,, \quad \gamma_{a_1} = 460(8)\,\mathrm{MeV}\,, \quad |\kappa| = 0.14(1)\,, \quad \mathcal{N} = 1.10(4)\,, \tag{4.6}$$

with a $\chi^2/\mathrm{dof} = 2.83$ for the mode $\tau^- \to \pi^-\pi^+\pi^-\nu_\tau$.

These results bring us to a first observation that is that, in general, the agreement between our models and ALEPH data is better for $\tau^- \to \pi^-\pi^0\pi^0\nu_\tau$ than for $\tau^- \to \pi^-\pi^+\pi^-\nu_\tau$ as indicated by the χ^2/d.o.f. We also observe that the overall normalization with the model without the inclusion of the a_1' needs an unnaturally large correction $\sim (40-60)\%$ to match experimental data, while if this resonance is included, the χ^2/dof is slightly better and the required normalization factor reduces to 1.21 and 1.10 for the $\pi^-\pi^0\pi^0$ and $\pi^-\pi^+\pi^-$ modes, respectively.

We next run fits with the dispersive Breit-Wigner form factor presented in Eqs. (3.10) and (3.14). Regarding the integral cutoff s_{cut} in Eq. (3.12), one should take a value as large as possible so as not to spoil the *a priori* infinite interval of integration, but low enough that the running width is well known within the interval. The parameters resulting from the fits are collected in Table 1 as Fit-a_1 and Fit-a_1', respectively, for the model including only the a_1 and both the a_1 and a_1' axial resonances. The dependence of the fitted parameters on s_{cut} is explored for three representative values of s_{cut}, namely 4 GeV^2, 9 GeV^2 and 100 GeV^2. One observes that only the a_1-width is sensitive to these variations with a tendency of becoming larger as s_{cut} increases, the rest of parameters remain rather stable. Despite this issue represents a source of systematic (model-dependent) uncertainty with regard to the treatment of the a_1-meson resonance parameters, slightly better fits are obtained with $s_{\mathrm{cut}} = 100$ GeV^2 as the χ^2/dof indicates. We have also tried larger values of s_{cut} i.e. 1000 GeV^2 or 10000 GeV^2, and found that while the numerical value for the a_1-width still suffers positive variations of some MeV, the χ^2/dof remains stable. Therefore, we consider the parameters obtained with $s_{\mathrm{cut}} = 100$ GeV^2 as our reference fits. Although this choice it may not be rigorous, the quality of the present data is not precise enough to disentangle these effects. As seen from the table, the value for the a_1 mass(width) is slightly shifted upwards(downwards) with respect to non-dispersive model as a consequence of including the running mass in the parametrization. Also, the fit parameters are found to be much more stable against the inclusion of the a_1'. However, the most important improvements are seen in the goodness of the χ^2/dof of the $\pi^-\pi^+\pi^-$ decay, which has been reduced by $\sim 50\%$, and in the normalization factor $\mathcal{N}$. For the $\pi^0\pi^0\pi^-$ decay channel one observes that, due to the satisfactory quality of the fit, the fit parameter $\mathcal{N} = 0.97(3)$ is found to

Fit	Decay channel	$s_{\rm cut}$ [GeV^2]	m_{a_1} [MeV]	γ_{a_1} [MeV]	$\mathcal{N}$	$\|\kappa\|$	χ^2/dof
Fit-a_1	$\pi^0\pi^0\pi^-$	4	1293(5)	416(6)	0.84(2)	—	1.07
		9	1293(5)	448(7)	0.87(2)	—	1.02
		100	1293(5)	501(9)	0.88(2)	—	1.01
	$\pi^-\pi^+\pi^-$	4	1256(3)	395(5)	0.77(1)	—	1.61
		9	1259(3)	426(6)	0.80(1)	—	1.53
		100	1259(4)	474(7)	0.81(2)	—	1.51
Fit-a_1'	$\pi^0\pi^0\pi^-$	4	1289(5)	404(7)	0.92(3)	0.11(4)	0.97
		9	1291(5)	434(8)	0.96(3)	0.12(4)	0.88
		100	1293(4)	485(10)	0.97(3)	0.12(4)	0.86
	$\pi^-\pi^+\pi^-$	4	1256(3)	390(6)	0.80(2)	0.03(2)	1.60
		9	1259(3)	420(6)	0.84(2)	0.05(2)	1.47
		100	1260(3)	467(8)	0.85(2)	0.05(2)	1.43

Table 1. Results for the fits to the 2014 ALEPH $\tau^- \to (3\pi)^-\nu_\tau$ axial spectral function data [30] obtained with the dispersive Breit-Wigner representations Eqs. (3.10) and (3.14) including, respectively, only the $a_1(1260)$ (Fit-a_1) and both the $a_1(1260)$ and $a_1(1640)$ (Fit-a_1') axial resonances, for three representative values of $s_{\rm cut}$ in the dispersive integral Eq. (3.12).

be very well compatible with data i.e. $\mathcal{N}=1$. On the contrary, the $\pi^-\pi^+\pi^-$ mode needs to be corrected by a scale factor of $\mathcal{N}=0.85(2)$.

In Figs. 1 and 2, we provide a graphical account of the results of our fits compared to ALEPH data[7]. In particular, the results of the fits given in Eqs. (4.3) and (4.4) obtained with the non-dispersive Breit-Wigner model are shown by the dashed blue curve for the $\pi^0\pi^0\pi^-$ (solid black circles) and $\pi^-\pi^+\pi^-$ (solid red squares) decay channels in Figs. 1 and 2, respectively. In these plots, we also display the fits presented in Table 1 resulting from the application of the dispersive Breit-Wigner description with one (dotted and dot-dashed green curves for the $\pi^0\pi^0\pi^-$ and $\pi^-\pi^+\pi^-$ modes, respectively) and two (solid red and black curves) axial-vector resonances. Comments on the effects of including the running mass are in order: *i*) the description of the low-energy data points is slightly improved (see the insets in Figs. 1 and 2); *ii*) the peak is seen slightly shifted to the left; *iii*) the description of the second half of the spectral function is found to be slightly over the non-dispersive ones. In all, the agreement with data is found to be quite satisfactory.

Let us discuss next the individual a_1 and a_1' contributions in more detail. In Figs. 3 and 4, we display our fit results obtained with the dispersive Breit-Wigner representation including both the $a_1(1260)$ and $a_1(1640)$ axial meson resonances, together with their individual contributions. While the total contribution is given by the solid curves in the figures, that result in a total branching ratio of

$$\mathrm{BR}(\tau^- \to \pi^0\pi^0\pi^-\nu_\tau) = 9.32()\%\,, \quad \mathrm{BR}(\tau^- \to \pi^-\pi^+\pi^-\nu_\tau) = 9.05()\%\,, \qquad (4.7)$$

[7]Notice that in the figures we have kept the corresponding normalization factors in order to compare the shapes of the spectral function.

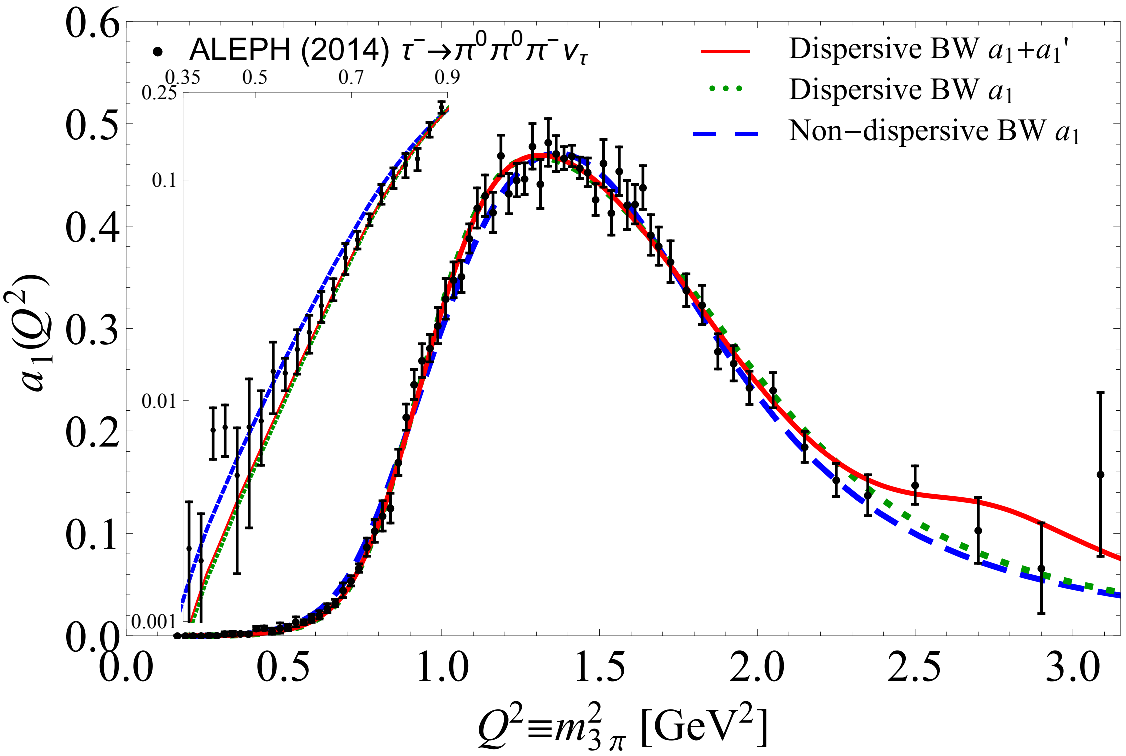

Figure 1. ALEPH 2014 measurements [30] of the axial spectral function from $\tau^- \to \pi^0\pi^0\pi^-\nu_\tau$ (solid black circle) as compared to the fit results presented in Eq. (4.3), obtained with the non-dispersive Breit-Wigner including only the a_1 resonance according to Eq. (3.1) (dashed blue curve), and in Table 1, with the dispersive Breit-Wigner including one (dashed green curve) and two (solid red curve) axial resonances according to Eqs. (3.10) and (3.14), respectively. The inset shows a magnification of the respective fits in the region $Q^2 \in [0.35, 0.9]$ GeV^2 in logarithmic scale.

the resulting contribution of the $a_1(1260)$-meson to the spectral function is shown as the dashed curve, and its individual contribution to the branching ratio is found to be

$$\mathrm{BR}(\tau^- \to a_1\nu_\tau \to \pi^0\pi^0\pi^-\nu_\tau) = 10.56()\% \,, \quad \mathrm{BR}(\tau^- \to a_1\nu_\tau \to \pi^-\pi^+\pi^-\nu_\tau) = 9.61()\% \,. \tag{4.8}$$

The contribution of the $a_1(1640)$ is shown by the dotted curve in Figs. 3 and 4 for the central values of $|\kappa| = 0.12$ and $|\kappa| = 0.05$ given in Table 1; let us remind that for the a_1' mass and width we have employed the PDG values. Notice that, although the individual contribution of the a_1' is found to be small,

$$\mathrm{BR}(\tau^- \to a_1'\nu_\tau \to \pi^0\pi^0\pi^-\nu_\tau) = 1.0 \times 10^{-3} \,, \quad \mathrm{BR}(\tau^- \to a_1'\nu_\tau \to \pi^-\pi^+\pi^-\nu_\tau) = 1.7 \times 10^{-4} \,, \tag{4.9}$$

its effect is rather important due to the destructive interference with the dominant a_1 resonance. As seen, the individual a_1' contribution turns out to be rather sensitive to the

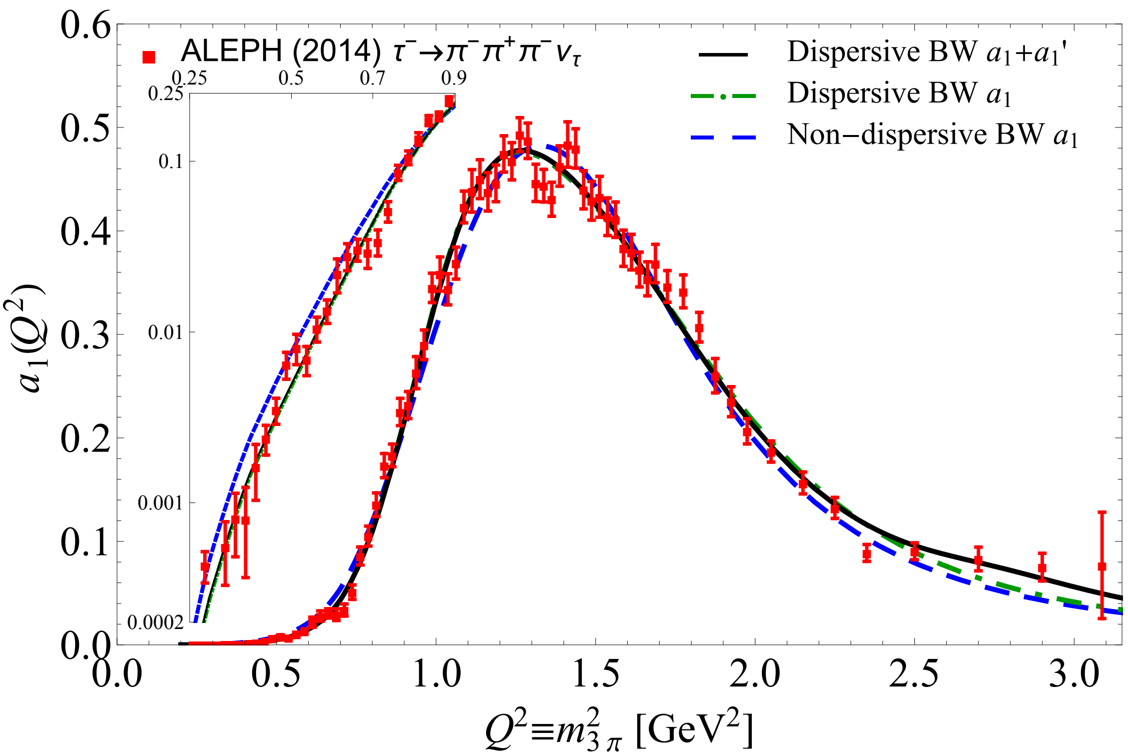

Figure 2. ALEPH 2014 measurements [30] of the axial spectral function from $\tau^- \to \pi^-\pi^+\pi^-\nu_\tau$ (solid red square) as compared to the fit results presented in Eq. (4.4) obtained with the non-dispersive Breit-Wigner including only the a_1 resonance according to Eq. (3.1) (dashed blue curve), and in Table 1 with the dispersive Breit-Wigner including one (dor-dashed green curve) and two (solid black curve) axial resonances according to Eqs. (3.10) and (3.14), respectively. The inset shows a magnification of the respective fits in the region $Q^2 \in [0.25, 0.9]$ GeV^2 in logarithmic scale.

mixing parameter $|\kappa|$ (cf. Eq. (3.14)). It is difficult to asses a precise value for κ, but an estimate can be inferred adjusting κ such that the experimental branching ratios reported by ALEPH, $\mathrm{BR}(\tau^- \to \pi^0\pi^0\pi^-\nu_\tau) = 9.239\%$ and $\mathrm{BR}(\tau^- \to \pi^-\pi^+\pi^-\nu_\tau) = 9.041\%$, are reproduced. As an exercise, we fix both the mass and width of the a_1 and a_1' to their PDG values, and we find that κ is positive, $\kappa \approx 0.26$ and $\kappa \approx 0.29$. These values are in reasonable agreement with, although slightly larger than, our findings of Table 1.

To make our work self-contained, in Fig. 5, our expressions for the running mass (cf. Eq. (3.7)) and width (cf. Eq. (3.2)) are plotted as a function of the 3π invariant mass for the nominal values $m_{a_1} = 1293(5)$ MeV and $\gamma_{a_1} = 501(9)$ MeV obtained from the $\pi^0\pi^0\pi^-$ mode Fit-a_1 in Table 1.

We have also performed a simultaneous fit to both decay channels. The corresponding results are found to be

$$m_{a_1} = 1270(3)\,\mathrm{MeV}\,, \quad \gamma_{a_1} = 480(5)\,\mathrm{MeV}\,, \quad \mathcal{N} = 0.83(1)\,, \tag{4.10}$$

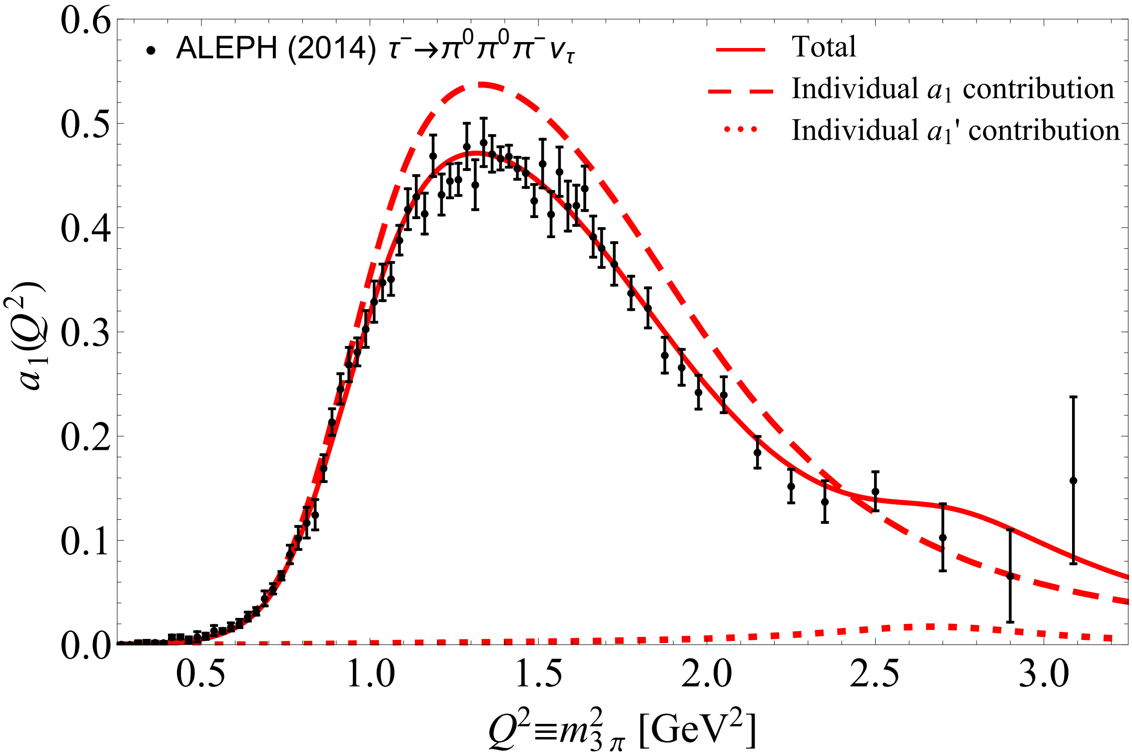

Figure 3. ALEPH 2014 measurements [30] of the axial spectral function from $\tau^- \to \pi^0\pi^0\pi^-\nu_\tau$ (solid black circles) as compared to the fit results obtained with the dispersive Breit-Wigner including two axial resonances according to Eq. (3.14), together with the individual contributions from the $a_1(1260)$ (dashed red lines) and $a_1(1640)$ (dotted red lines) axial mesons.

with a $\chi^2/\text{dof} = 1.57$ for Fit-a_1, and

$$m_{a_1} = 1271(3)\,\text{MeV}\,, \quad \gamma_{a_1} = 473(5)\,\text{MeV}\,, \quad \mathcal{N} = 0.87(2)\,, \tag{4.11}$$

with a $\chi^2/\text{dof} = 1.50$ for Fit-a_1'. The fit parameters tend to lie in between the individual fit results of both channels with a little preference to those of the $\pi^-\pi^+\pi^-$ mode as also indicated by the χ^2/dof. As a matter of example, the corresponding results for Fit-a_1 are displayed in Fig. 6 where we compare the dispersive Breit-Wigner fit results to the individual $\pi^0\pi^0\pi^-$ (dotted green curve) and $\pi^-\pi^+\pi^-$ (dot-dashed green curve) decay modes together with the outcome from the simultaneous fit (solid purple curve) to both data sets. As seen, the curve of the joint fit tends to that of the $\pi^-\pi^+\pi^-$, in line with the results of Table 1.

5 Dispersive fits to the ALEPH spectral function data

Our central fit results are obtained from the general solution of the dispersive representation presented in Eq. (3.19). In particular, we employ a twice subtracted dispersion relation

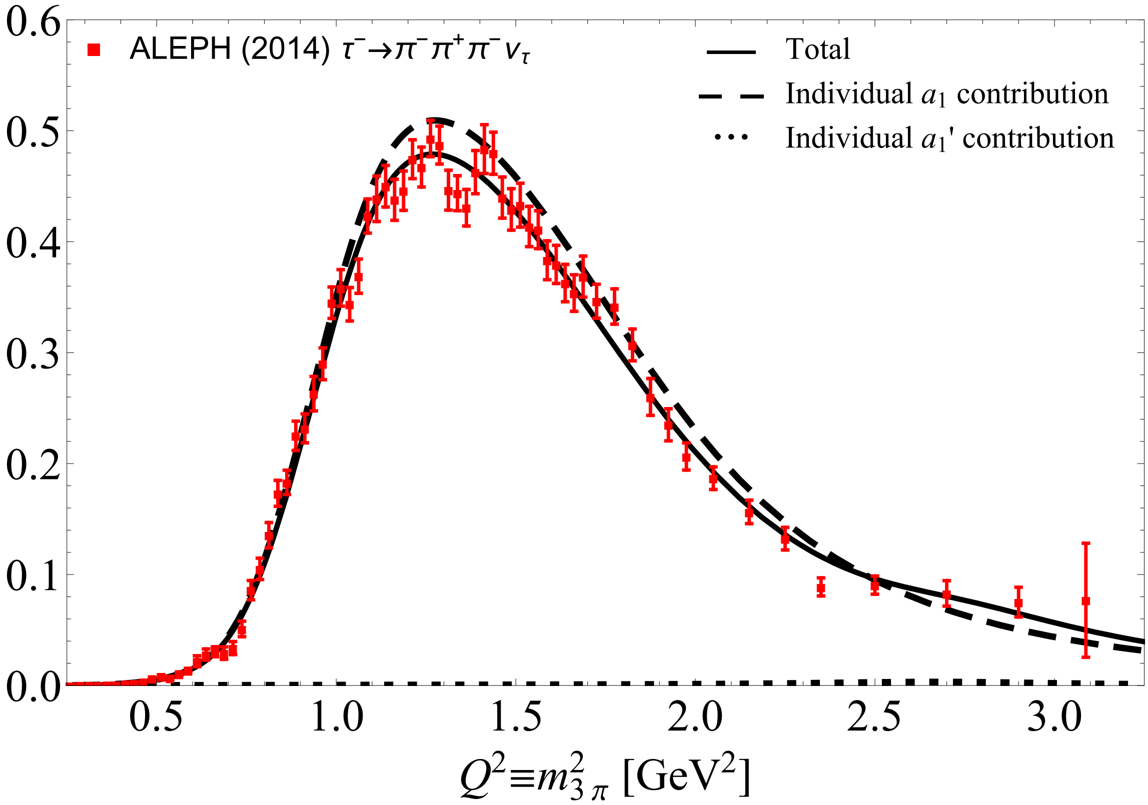

Figure 4. ALEPH 2014 measurements [30] of the axial spectral function from $\tau^- \to \pi^-\pi^+\pi^-\nu_\tau$ (solid red squares) as compared to the fit results obtained with the dispersive Breit-Wigner including two axial resonances according to Eq. (3.14), together with the individual contributions from the $a_1(1260)$ (dashed black lines) and $a_1(1640)$ (dotted black lines) axial mesons.

$(n = 2)$ at $s_0 = 0$. In this case, the form factor takes the form:

$$f(Q^2) = \exp\left[\alpha_1 Q^2 + \frac{Q^4}{\pi}\int_{9m_\pi^2}^{s_{\rm cut}} ds' \frac{\delta(s')}{(s')^2(s'-Q^2-i0)}\right], \tag{5.1}$$

where α_1 is a subtraction constant that can be related to low-energy observables appearing in the low-energy expansion of the form factor (cf. Eq. (2.37))

$$f(Q^2) = 1 + \lambda_1 Q^2 + \cdots . \tag{5.2}$$

Explicitly, the relation for the linear slope parameter λ_1 reads

$$\lambda_1 = \alpha_1 . \tag{5.3}$$

This subtraction constant can be calculated theoretically through the sum rule

$$\alpha_k^{\rm s.r.} = \frac{k!}{\pi}\int_{9m_\pi^2}^{s_{\rm cut}} ds' \frac{\delta(s')}{s'^{k+1}} . \tag{5.4}$$

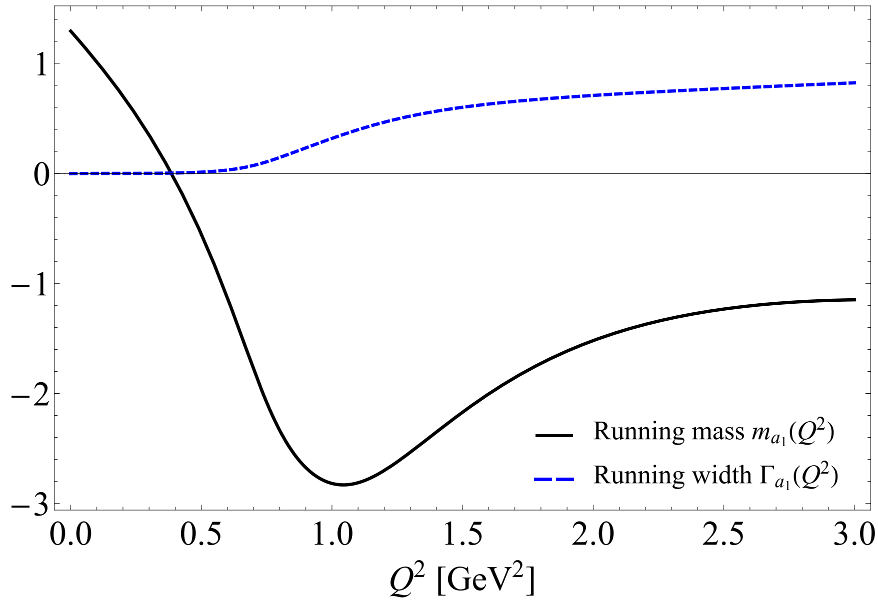

Figure 5. Running mass (solid black curve) and width (dashed blue curve) as a function of the invariant mass of the 3π system according to Eqs. (3.7) and (3.2), respectively.

As seen, the calculation of the subtraction constants from the sum rules depends in nothing else than on the perfect knowledge of the input phase $\delta(Q^2)$, knowledge that we do not have until infinity. Therefore, for our analysis, we treat them as free parameters to be determined from fits to data. This has the advantage that they turn out to be less model dependent and absorbs the effects of other possible production mechanisms different than the ones considered here-as they are in the data. In summary, the introduced subtraction constant encodes the low-energy physics but also capture our ignorance of the high-energy part of the dispersive integral, where the phase is less well know, thus showing a nice synergy between high-and low-energy regimes.

The contribution of the high-energy region of the dispersive integral can be studied through the cutoff $s_{\rm cut}$ introduced in Eq. (5.1) as the upper limit of integration. The resulting fit parameters with a twice-subtracted dispersion relation are given in Table 2 employing three values of $s_{\rm cut}$, namely 4 GeV^2, 9 GeV^2 and $s_{\rm cut} \to \infty$. As one observes, the dependence of the resulting fit parameters on $s_{\rm cut}$ is in general small and within uncertainties, though visible. In this table, we also show the subtraction constant $\alpha_1^{\rm s.r.}$ calculated through the sum rule Eq. (5.4), and the values we get are found to be in a reasonable agreement with the results of the fits. This indicates that the content of the phase is such that saturates rather well the dispersive integral, otherwise the differing results among them would be larger. Compared with the fits of Table 1, which employed a dispersive Breit-Wigner, while the χ^2/dof is practically unchanged, although now it remains slightly below, the normalization $\mathcal{N}$ turns out to be well compatible with data.

A graphical account of our central fit results is shown in Figs. 7 and 8 for the $\pi^0\pi^0\pi^-$ and $\pi^-\pi^+\pi^-$ decay modes, respectively. The solid lines correspond to the fit of Table 2

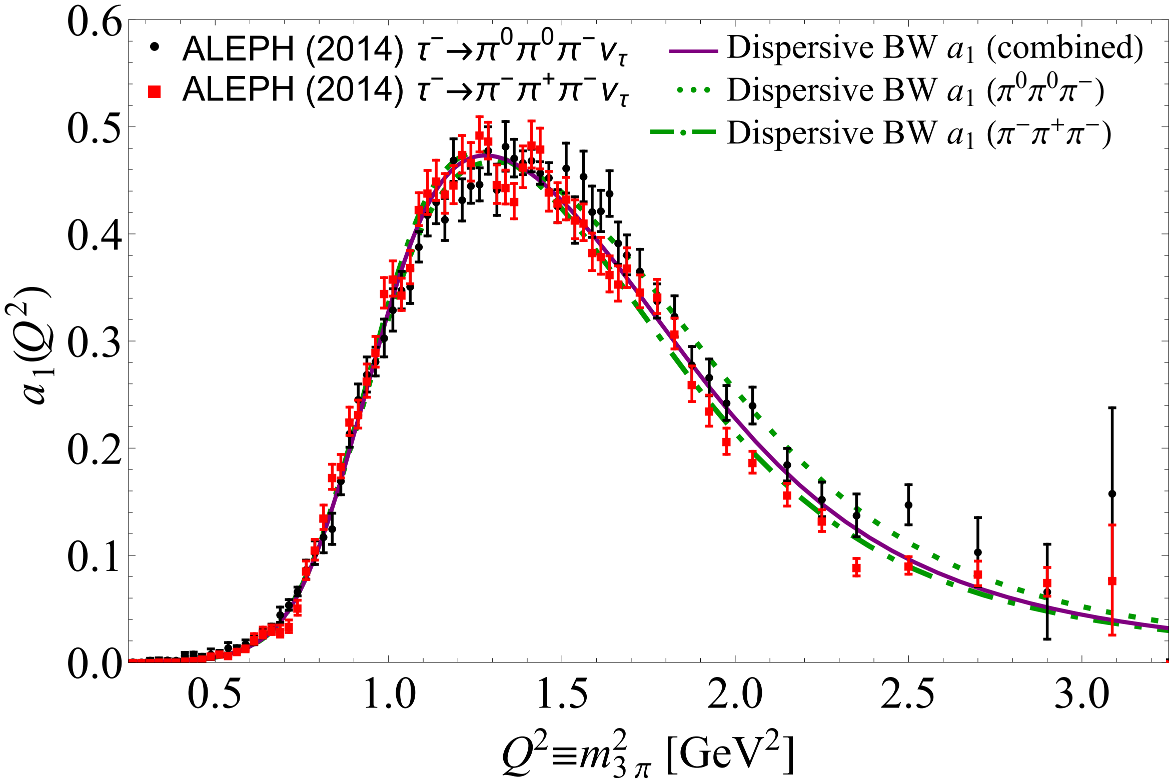

Figure 6. Simultaneous fit (solid purple curve) to both decay channels $\tau^- \to \pi^0\pi^0\pi^-\nu_\tau$ (solid black circle) and $\tau^- \to \pi^-\pi^+\pi^-\nu_\tau$ (solid red square) as compared to the individual fit results.

Fit	Channel	Parameter	$s_{\rm cut} = 4$ GeV^2	$s_{\rm cut} = 9$ GeV^2	$s_{\rm cut} \to \infty$
Fit-a_1	$\pi^0\pi^0\pi^-$	m_{a_1} [MeV]	1336(5)	1321(8)	1319(8)
		γ_{a_1} [MeV]	532(10)	489(10)	486(10)
		α_1 [GeV^{-2}]	0.66(3)	0.52(4)	0.49(4)
		$\alpha_1^{\rm s.r.}$ [GeV^{-2}]	0.39(1)	0.52(1)	0.63(1)
		$\mathcal{N}$	1.02(8)	1.22(12)	1.24(12)
		χ^2/dof	1.07	0.91	0.90
	$\pi^-\pi^+\pi^-$	m_{a_1} [MeV]	1280(3)	1271(7)	1270(7)
		γ_{a_1} [MeV]	503(2)	477(4)	474(7)
		α_1 [GeV^{-2}]	0.75(1)	0.64(3)	0.61(3)
		$\alpha_1^{\rm s.r.}$ [GeV^{-2}]	0.43(1)	0.56(1)	0.66(1)
		$\mathcal{N}$	0.78(3)	0.90(7)	0.93(7)
		χ^2/dof	1.61	1.50	1.49

Table 2. Results for the fits to the 2014 ALEPH $\tau^- \to (3\pi)^-\nu_\tau$ axial spectral function data [30] obtained with the dispersive representation Eqs. (5.1) including the $a_1(1260)$-meson axial resonance, for three representative values of $s_{\rm cut}$ in the dispersive integral.

with $s_{\rm cut} \to \infty$. As it can be see, our model provides a very good description of the ALEPH experimental data. In these plots, we also display the results obtained in Table 1 with the single resonance dispersive Breit-Wigner for comparison.

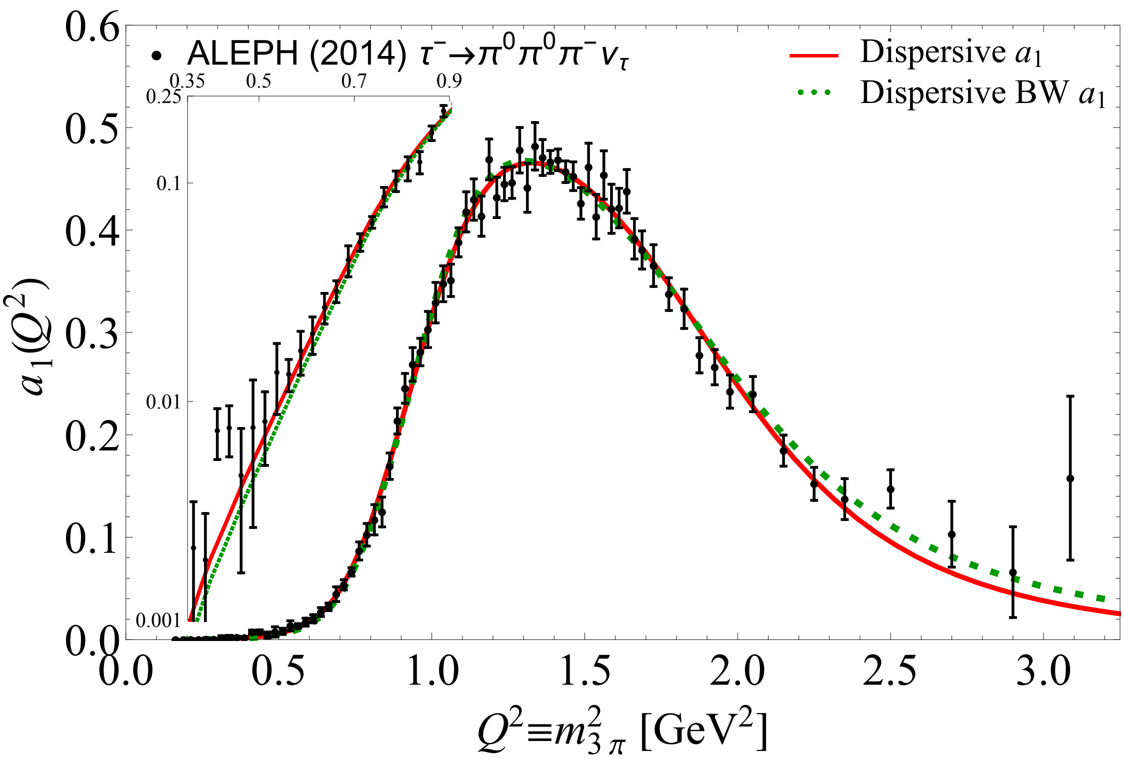

Figure 7. ALEPH 2014 measurements [30] of the axial spectral function from $\tau^- \to \pi^0\pi^0\pi^-\nu_\tau$ (solid black circle) as compared to the fit results presented in Table 2 for $s_{\rm cut} \to \infty$ (solid red line) and Table 1 with the single resonance dispersive Breit-Wigner (dotted green line). The inset shows a magnification of the respective fits in the region $Q^2 \in [0.35, 0.9]$ GeV^2 in logarithmic scale.

Finally, in Fig. 9 we take a closer look to the low-energy region of the spectral function. We can see that while the low-energy data points of the decay $\tau^- \to \pi^0\pi^0\pi^-\nu_\tau$ carry a large error bar and show some scatter, the data for the $\pi^-\pi^+\pi^-$ mode is more precise and is reasonably well accommodated within our description (solid purple curve) resulting from the simultaneous fit to both decay channel data sets. In this figure, the tree-level calculation in ChPT at LO (dotted gray line) and NLO (dot-dashed gray line), with the use of Eqs. (2.25) and (2.32), respectively, are also shown for illustrative purposes. As seen, while the ChPT prediction at NLO is able to accommodate the low-energy data of the $\pi^-\pi^+\pi^-$ decay channel, it fails from $Q^2 \sim 0.4$ GeV^2 on where the effects of the a_1 resonance contribution starts showing up.

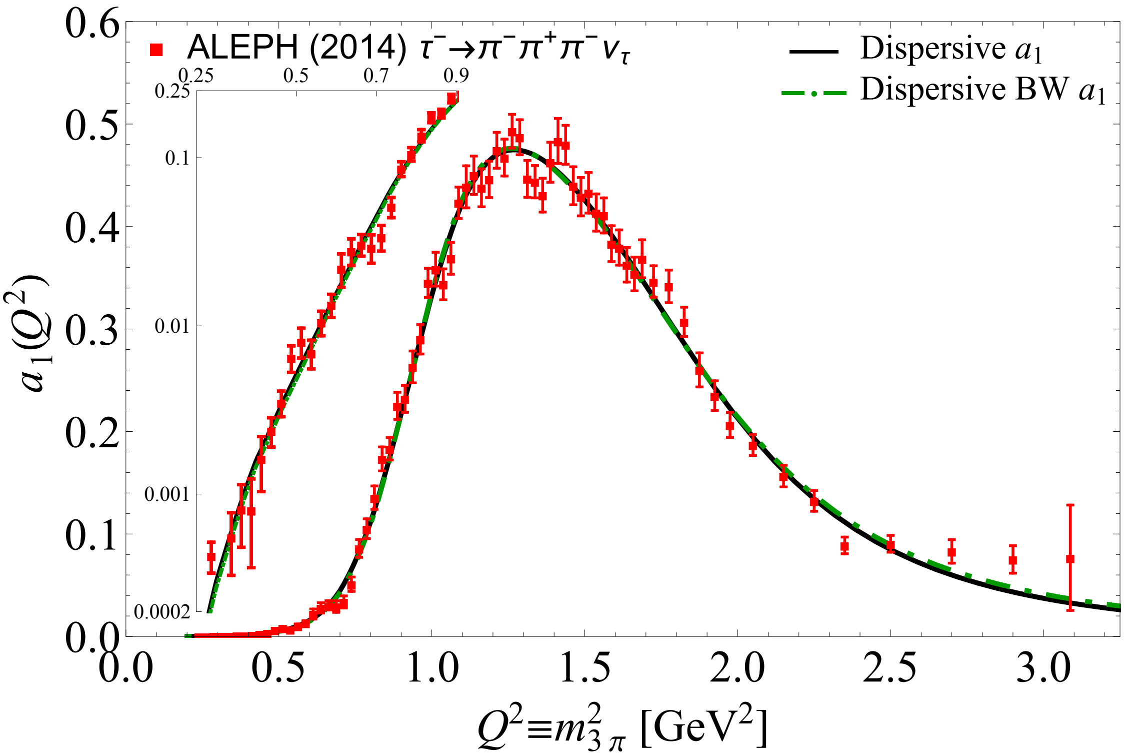

Figure 8. ALEPH 2014 measurements [30] of the axial spectral function from $\tau^- \to \pi^-\pi^+\pi^-\nu_\tau$ (solid red square) as compared to the fit results presented in Table 2 for $s_{\rm cut} \to \infty$ (solid black line) and Table 1 with the single resonance dispersive Breit-Wigner (dot-dashed green line). The inset shows a magnification of the respective fits in the region $Q^2 \in [0.25, 0.9]$ GeV^2 in logarithmic scale.

6 Conclusions

Hadronic tau decays constitute an advantageous laboratory to study the low-energy regime of QCD. In this work, we have analyzed the $\tau^- \to (3\pi)^-\nu_\tau$ axial-vector spectral function experimental data reported by ALEPH in 2014. These decays offer a good environment to study the strong dynamics of the three-pion system under rather clean conditions. This is expected to be dominated by the axial $a_1(1260)$-meson resonance and, therefore, the measured axial-vector spectral function allows one to study its properties and test models for the participant axial-vector form factor. For its description, we have explored several models which incorporate the constraints posed by analyticity and unitarity in an increasing degree of soundness. We have found that a satisfactory description of experimental data is achieved working with a twice-subtracted dispersion relation and without the need to include further intermediate states beyond the contributions of the $\rho(770)$, $a_1(1260)$ and $a_1(1640)$ resonances. Furthermore, we have investigated the contribution of the high-energy region of the dispersive integral through the introduction of a cutoff $s_{\rm cut}$ as the upper limit of integration. This cutoff was varied between 4 GeV^2 and infinity in order to test the sensitivity of the model for the form factor phase that we have used as input to contributions

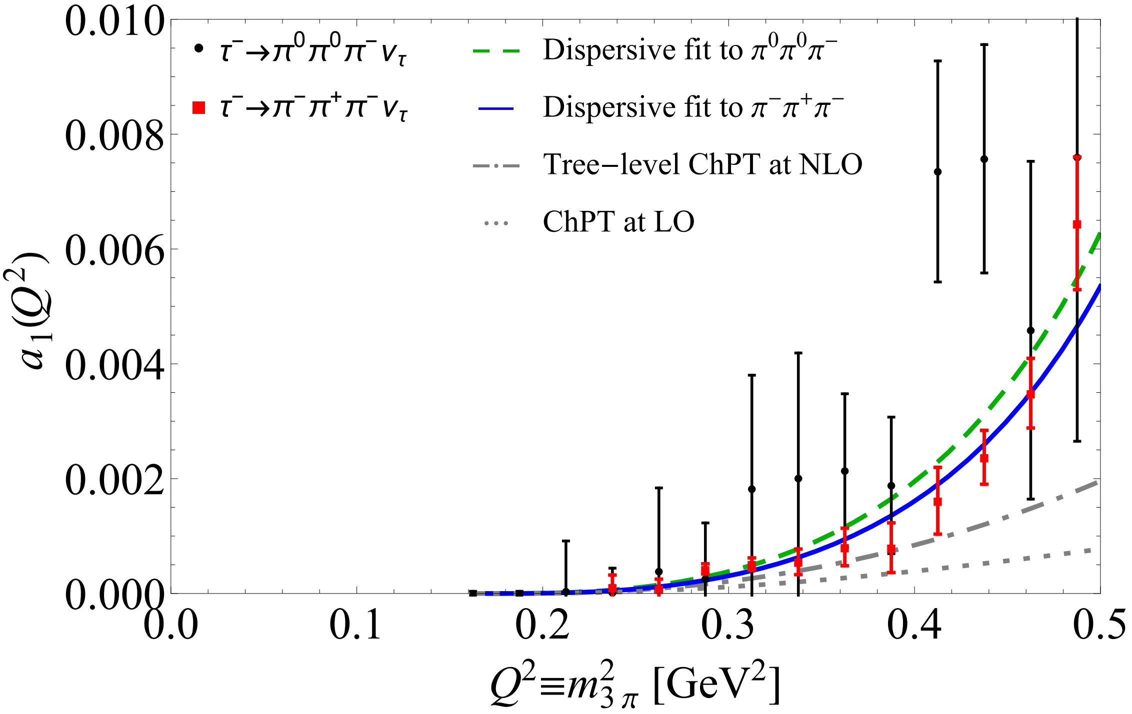

Figure 9. ALEPH 2014 measurements [30] of the axial spectral function from $\tau^- \to \pi^0\pi^0\pi^-\nu_\tau$ (solid black circle) and $\tau^- \to \pi^-\pi^+\pi^-\nu_\tau$ (solid red square) as compared to the fit results presented in Table 2 for $s_{\rm cut} \to \infty$. The tree-level ChPT calculation at leading-and-next-to-leading order are also shown for illustration (dotted and dot-dashed gray lines, respectively).

coming from higher-energies where the phase is not well-known.

Acknowledgments

The work of S.G-S has been supported by the National Science Foundation (Grant No. PHY-1714253). The work of E.P. is supported in part by the U.S. Department of Energy (contract DE-AC05-06OR23177) and by the National Science Foundation (Grant No. PHY-1714253).

References

[1] A. Friedland, S. Gonzàlez-Solís, E. Passemar, K. Quirion, *in preparation.*

[2] S. R. Amendolia *et al.* [NA7 Collaboration], Nucl. Phys. B **277**, 168 (1986).

[3] A. Aloisio *et al.* [KLOE Collaboration], Phys. Lett. B **606**, 12 (2005) [hep-ex/0407048].

[4] R. R. Akhmetshin *et al.* [CMD-2 Collaboration], Phys. Lett. B **648**, 28 (2007) [hep-ex/0610021].

[5] B. Aubert *et al.* [BaBar Collaboration], Phys. Rev. Lett. **103**, 231801 (2009) [arXiv:0908.3589 [hep-ex]].

[6] F. Ambrosino *et al.* [KLOE Collaboration], Phys. Lett. B **700**, 102 (2011) [arXiv:1006.5313 [hep-ex]].

[7] M. Ablikim *et al.* [BESIII Collaboration], Phys. Lett. B **753**, 629 (2016) [arXiv:1507.08188 [hep-ex]].

[8] A. Anastasi *et al.* [KLOE-2 Collaboration], JHEP **1803**, 173 (2018) [arXiv:1711.03085 [hep-ex]].

[9] S. Anderson *et al.* [CLEO Collaboration], Phys. Rev. D **61**, 112002 (2000) [hep-ex/9910046].

[10] M. Fujikawa *et al.* [Belle Collaboration], Phys. Rev. D **78**, 072006 (2008) [arXiv:0805.3773 [hep-ex]].

[11] S. Gonzàlez-Solís and P. Roig, Eur. Phys. J. C **79**, no. 5, 436 (2019) [arXiv:1902.02273 [hep-ph]].

[12] C. Adolph *et al.* [COMPASS Collaboration], Phys. Rev. D **95**, no. 3, 032004 (2017) [arXiv:1509.00992 [hep-ex]].

[13] S. Eideleman (Particle Data Group), "The $a_1(1260)$ and $a_1(1640)$" (2003).

[14] H. Albrecht *et al.* [ARGUS Collaboration], Z. Phys. C **58**, 61 (1993).

[15] R. Barate *et al.* [ALEPH Collaboration], Eur. Phys. J. C **4**, 409 (1998).

[16] P. Abreu *et al.* [DELPHI Collaboration], Phys. Lett. B **426**, 411 (1998).

[17] K. Ackerstaff *et al.* [OPAL Collaboration], Z. Phys. C **75**, 593 (1997).

[18] D. M. Asner *et al.* [CLEO Collaboration], Phys. Rev. D **61**, 012002 (2000) [hep-ex/9902022].

[19] T. E. Browder *et al.* [CLEO Collaboration], Phys. Rev. D **61**, 052004 (2000) [hep-ex/9908030].

[20] N. A. Tornqvist, Z. Phys. C **36**, 695 (1987) Erratum: [Z. Phys. C **40**, 632 (1988)].

[21] N. Isgur, C. Morningstar and C. Reader, Phys. Rev. D **39**, 1357 (1989).

[22] J. H. Kuhn and A. Santamaria, Z. Phys. C **48**, 445 (1990).

[23] M. Feindt, Z. Phys. C **48**, 681 (1990).

[24] D. Gomez Dumm, A. Pich and J. Portoles, Phys. Rev. D **69**, 073002 (2004) [hep-ph/0312183].

[25] D. G. Dumm, P. Roig, A. Pich and J. Portoles, Phys. Lett. B **685**, 158 (2010) [arXiv:0911.4436 [hep-ph]].

[26] S. Schael *et al.* [ALEPH Collaboration], Phys. Rept. **421**, 191 (2005) [hep-ex/0506072].

[27] M. Vojik and P. Lichard, arXiv:1006.2919 [hep-ph].

[28] P. Lichard, arXiv:1703.06315 [hep-ph].

[29] M. Mikhasenko *et al.* [JPAC Collaboration], Phys. Rev. D **98**, no. 9, 096021 (2018) [arXiv:1810.00016 [hep-ph]].

[30] M. Davier, A. Höcker, B. Malaescu, C. Z. Yuan and Z. Zhang, Eur. Phys. J. C **74**, no. 3, 2803 (2014) [arXiv:1312.1501 [hep-ex]].

[31] A. Pich and J. Portolés, Phys. Rev. D **63**, 093005 (2001) [hep-ph/0101194].

[32] D. Gómez Dumm and P. Roig, Eur. Phys. J. C **73**, no. 8, 2528 (2013) [arXiv:1301.6973 [hep-ph]].

[33] D. R. Boito, R. Escribano and M. Jamin, Eur. Phys. J. C **59**, 821 (2009) [arXiv:0807.4883 [hep-ph]].

[34] P. Roig, arXiv:1301.7626 [hep-ph].

[35] L. Girlanda and J. Stern, Nucl. Phys. B **575**, 285 (2000) [hep-ph/9906489].

[36] J. J. Sanz-Cillero and O. Shekhovtsova, JHEP **1712**, 080 (2017) [arXiv:1707.01137 [hep-ph]].

[37] M. Tanabashi *et al.* [Particle Data Group], Phys. Rev. D **98**, 030001 (2018).

[38] A. Celis, V. Cirigliano and E. Passemar, Phys. Rev. D **89**, 013008 (2014) [arXiv:1309.3564 [hep-ph]].

[39] R. Fischer, J. Wess and F. Wagner, Z. Phys. C **3**, 313 (1979).

[40] G. Colangelo, M. Finkemeier and R. Urech, Phys. Rev. D **54**, 4403 (1996) [hep-ph/9604279].

[41] G. Ecker, J. Gasser, A. Pich and E. de Rafael, Nucl. Phys. B **321**, 311 (1989).

[42] R. Omnes, Nuovo Cim. **8**, 316 (1958).